Article

Adsorption configuration control on Pt-Bi$_2$O$_3$ for the oriented conversion of glycerol to glyceric acid via terminal hydroxyl oxidation

Han-Yue Yang, Bin Sun, Xue Xiao *, Xuan Ai *, Rui-Bin Jiang, Pei Chen, Yu Chen *

Key Laboratory of Macromolecular Science of Shaanxi Province, Shaanxi Key Laboratory for Advanced Energy Devices, Shaanxi Engineering Lab for Advanced Energy Technology, School of Materials Science and Engineering, Shaanxi Normal University, Xi'an 710062, China

ABSTRACT

Glycerol, a byproduct of biodiesel production, can be efficiently converted into valuable chemicals through electrocatalytic reaction. In this study, platinum (Pt) nanocrystals decorated on bismuth oxide (Bi$_2$O$_3$) nanosheets (PtBi DONS) with an optimal Pt:Bi ratio of 1:1 were successfully synthesized using a galvanic replacement method. Pt$_1$Bi$_1$ DONS exhibit remarkable electrocatalytic performance for glycerol electrooxidation, achieving an excellent catalytic activity (current of 0.82 A mg$_{Pt}^{-1}$ at 0.67 V vs. reversible hydrogen electrode (RHE)) and an exceptional selectivity of 96.6% for C$_3$ products, particularly glyceric acid. The superior performance stems from two key factors: (1) electron transfer from Bi$_2$O$_3$ to Pt creates electron-rich Pt sites that suppress C–C bond cleavage and (2) Bi$_2$O$_3$ facilitates favorable glycerol adsorption configurations through multiple hydroxyl group interactions. Mechanistic studies using *operando* spectroscopy and electrochemical impedance spectroscopy revealed that the synergistic effect between Pt and Bi$_2$O$_3$ promotes rapid charge transfer and stable intermediate formation. Moreover, PtBi DONS showed excellent versatility in oxidizing other polyols compared with monoalcohols.

© 2025 The Authors. Published by Elsevier B.V. and Science China Press. All rights are reserved, including those for text and data mining, AI training, and similar technologies.

1. Introduction

Glycerol emerges as a notable byproduct in the biodiesel production process, accounting for ~10% of total output by weight [1–3]. As biodiesel offers a sustainable alternative to conventional fossil fuels owing to its renewable, nontoxic, and biodegradable nature, the resultant excess supply of glycerol has outstripped the current market demand, consequently affecting its economic viability [4–6]. This scenario has driven considerable interest in transforming glycerol into higher-value chemicals [7]. Glycerol oxidation yields a spectrum of products [8] from those maintaining the original C$_3$ carbon backbone to smaller C$_2$ and C$_1$ structures derived from one and two C–C bond cleavages [9]. Among various glycerol derivatives, C$_3$ products, such as glyceraldehyde (GLAD), dihydroxyacetone (DHA), and glyceric acid (GLA), have high economic value [10]. In particular, GLA has garnered attention owing to its application in the food, pharmaceutical, and cosmetic industries and its potential as a precursor for biodegradable polymers and other fine chemicals [11–13]. Therefore, utilizing excess and

low-cost glycerol to obtain higher-value products through electrochemical transformation [14] stands out as an innovative and environmentally friendly approach for upgrading glycerol.

Platinum (Pt) is regarded as one of the most efficacious electrocatalysts for glycerol oxidation reaction (GOR) owing to its advantageous electronic structure, particularly its low d-band center [15–17]. However, conventional Pt electrocatalysts exhibit inherent limitations substantially restricting their practical applications. First, the propensity for C–C bond cleavage on Pt surfaces can lead to the formation of considerable amounts of C$_1$ products, such as formic acid (FA) and carbon dioxide (CO$_2$); however, this occurs alongside the production of substantial C$_2$ and C$_3$ products, which challenges the selective formation of valuable C$_3$ products [15,17–19]. Second, the applied oxidation potential and the extended electrolysis time unavoidably result in the formation of Pt oxides [4,20], which impede the adsorption of hydroxyls and glycerol and consequently decrease the catalytic activity. In addition, the presence of carbonaceous residues, such as carbon monoxide (CO), represents a notable challenge to the catalytic performance as they occupy sites and block channels required for hydroxyl species interactions [4]. CO accumulation generally causes the poisoning effect, which in turn reduces the catalytic performance and selectivity of the C$_3$ products. It is, therefore, essential to develop

* Corresponding authors.
 E-mail addresses: xxiao@snnu.edu.cn (X. Xiao), aixuan@snnu.edu.cn (X. Ai), chenyu001@snnu.edu.cn (Y. Chen).

innovative approaches to enhance the adsorption and activation of hydroxyl species and organic molecules on Pt-based electrocatalysts [21]. Thus, improving these interactions is crucial for boosting the efficiency and selectivity of Pt-based electrocatalysts in GOR.

The co-adsorption of organic substrates and hydroxyl species is pivotal in achieving selective production of target chemicals [22]. Tailoring the adsorption capacity for hydroxyl species, along with optimizing glycerol adsorption configurations, enhances GOR activity and improves selectivity for C_3 products in alkaline media [21]. An increased concentration of hydroxyl species results in increased catalytic activity, which can be attributed to the high coverage and diffusion of hydroxyl species [23]. In general, hydroxyl species are more conducive to promoting the conversion of intermediates to carboxylates, given that the greater the number of hydroxyl and oxygen species that are adsorbed, the greater the barrier to the C–C bond cleavage [24–26]. While bismuth (Bi) and its oxides promote oxygenated species availability on Pt electrocatalysts [27,28] and dopants such as Bi [29,30], ruthenium (Ru) [31], and antimony (Te) [32] show high DHA selectivity, strategically modulating reaction pathways for GLA production remains a major challenge. In particular, the mechanistic role of Bi in directing GOR pathway selectivity and the potential for synergistic effects through rational catalyst design await comprehensive investigation.

Herein, Pt nanocrystals (Pt NC) decorated on bismuth oxide (Bi_2O_3) nanosheets (PtBi DONS) were synthesized using the galvanic replacement reaction. The ultrathin two-dimensional (2D) structure of Pt_1Bi_1 DONS offered a high surface area and efficient mass transfer pathways. The electrochemical analyses revealed that Pt_1Bi_1 DONS exhibited larger peak oxidation currents and more negative onset potentials (0.36 V vs. reversible hydrogen electrode (RHE)) for GOR than commercial Pt nanocrystals (cPt NC). Product assays indicated that Pt_1Bi_1 DONS achieved high selectivity for the conversion of glycerol to C_3 high-value chemicals, particularly GLA, comprising 88.3% of the C_3 products. Notably, the distinct electronic property of Pt_1Bi_1 DONS improved the selectivity for C_3 products, in which the electron-rich Pt helped in controlling the oxidation degree of the C–C bond. Furthermore, the presence of Bi_2O_3 facilitated the adsorption of OH_{ads} groups in the polyols to form a more stable adsorption conformation and promoted the rapid transfer of electrons.

2. Experimental

2.1. Materials

Bismuth nitrate pentahydrate ($Bi(NO_3)_3 \cdot 5H_2O$, ≥99.0%), bismuth(III) acetate ($Bi(C_2H_3O_2)_3$, ≥99.0%), ʟ-ascorbic acid (AA, $C_6H_8O_6$, ≥99.0%), 1-octadecene (ODE, $C_{18}H_{36}$, ≥90.0%), oleylamine (OAm, $C_{18}H_{37}N$, ≥99.5%) and mannitol ($C_6H_{14}O_6$, ≥98.0%) were purchased from Shanghai Aladdin Biochemical Technology Co., Ltd. Zinc pellets (Zn pellets, ≥99.0%) were purchased from Tianjin Kemiou Chemical Reagent Co., Ltd. Polyethylene glycol (Mw=600, PEG-600, ≥99.9%), platinum(II) acetylacetonate ($Pt(acac)_2$, ≥98.0%), hexadecyl trimethyl ammonium bromide (CTAB, ≥98.0%), potassium hydroxide (KOH, ≥99.0%), glycerol ($C_3H_8O_3$, ≥99.0%), methanol (CH_4O, ≥99.5%), and ethanol (C_2H_6O, ≥99.7%) were purchased from Sinopharm Chemical Reagent Co., Ltd. Ethylene glycol (($CH_2OH)_2$, ≥99.0%) was purchased from Tianjin Zhiyuan Chemical Reagent Co., Ltd. *n*-propanol (C_3H_8O, ≥99.8%) was purchased from Tianjin Fuyu Fine Chemical Co., Ltd. Potassium tetrachloroplatinate (II) (K_2PtCl_4, ≥99.9%) was purchased from Shanghai Chemical Reagent Co., Ltd. Commercial platinum nanocrystals (cPt NC) were purchased from Suzhou Sinero Technology Co., Ltd.

2.2. Synthesis of Pt_1Bi_1 DONS

Bi nanosheets (Bi NS) were synthesized according to a previously reported study [33]. Pt_1Bi_1 DONS were synthesized via a galvanic replacement reaction. In a typical procedure, an aqueous solution of K_2PtCl_4 (1.65 mL, 0.15 mol L^{-1}) was introduced into a Bi NS suspension (18 mL, 0.72 mg mL^{-1}), followed by brief ultrasonication (2 min) to ensure homogeneous mixing. The reaction mixture was maintained at room temperature under static conditions for 5 h. The resulting PtBi DONS were isolated by centrifugation (10,000 r min^{-1}, 2 min), followed by sequential washing with deionized water and ethanol to remove residual reactants. The final product was collected for further characterization. Pt_1Bi_3 DONS were obtained by varying the feeding amount of 0.15 mol L^{-1} K_2PtCl_4 solution while keeping the other conditions unchanged.

Further details regarding the methods can be found in the Supplementary material.

3. Results and discussion

3.1. Structural and compositional characterizations of Pt_1Bi_1 DONS

The galvanic replacement reaction between Bi nanosheets (Bi NS) and K_2PtCl_4 was employed to synthesize Pt_1Bi_1 DONS using the difference in standard electrode potentials between Bi ($E^{\ominus}$ (Bi^{3+}/Bi) = 0.308 V) and K_2PtCl_4 ($E^{\ominus}$ ($PtCl_4^{2-}$/Pt) = 0.755 V) (Fig. 1a). In this galvanic replacement reaction process, the presynthesized Bi NS synchronously serve as a reducing agent and a structural template. The spontaneous redox reaction results in a reduction of $PtCl_4^{2-}$ and the simultaneous oxidation of Bi, thereby leading to the formation of a distinctive nanosheet structure of Pt_1-Bi_1 DONS. The morphological characteristics of Pt_1Bi_1 DONS were elucidated through a comprehensive suite of microscopic and spectroscopic techniques. Transmission electron microscopy (TEM) analysis (Figs. 1b and Fig. S1 online) and high-angle annular dark-field electron microscopy (HAADF-STEM) (Fig. 1c) reveal that Pt_1Bi_1 DONS preserves the intrinsic skeletal structure of Bi NS. Atomic force microscopy (AFM) measurement (Fig. 1d) reveals an average thickness of 3.5 nm for Pt_1Bi_1 DONS, corroborating the ultrathin nature of the nanosheets as evidenced by TEM analysis. High-resolution TEM (HRTEM) analysis of Pt_1Bi_1 DONS reveals the distinct lattice fringes with d-spacings of 0.196 and 0.268 nm (Fig. 1e), which are associated with the Pt (200) and α-Bi_2O_3 (200) crystallographic planes, respectively. High-angle annular dark-field electron microscopy (HAADF-STEM) energy-dispersive X-ray spectroscopy (EDX) mapping (Fig. 1f) demonstrates the homogeneous dispersion of Pt NC throughout Bi_2O_3 nanosheets (Bi_2O_3 NS). Quantitative compositional analysis, performed using EDX and inductively coupled plasma atomic emission spectroscopy (ICP-OES), illustrates the Pt/Bi atomic ratio in Pt_1Bi_1 DONS to be 44.79:55.21 (Fig. S2a online) and 43.8:55.2 (Fig. S2b online).

To elucidate the crystallographic structure and phase composition of the synthesized Pt_1Bi_1 DONS, X-ray diffraction (XRD) analysis was conducted. The resulting diffractogram (Fig. 2a) reveals a complex pattern indicative of a multiphase system. Distinct diffraction peaks are observed at 39.7°, 46.2°, 67.5°, and 81.3°, which can be unambiguously indexed to the (111), (200), (220), and (311) lattice planes of face-centered cubic (fcc) Pt, respectively. These reflections align with the standard pattern of metallic Pt (JCPDS card No. 04-0802), indicating the successful reduction of K_2PtCl_4. In addition, the XRD pattern displays peaks at 27.4°, 33.3°, and 48.7°, matching the (120), (200), and (041) planes of the α-Bi_2O_3 phase (JCPDS No. 72-0398). Notably, these Bi_2O_3 reflections exhibit a slight downshift in Pt_1Bi_1 DONS, indicating the successful decoration of Pt NC on the surface of Bi_2O_3 NS. Meanwhile, the XRD

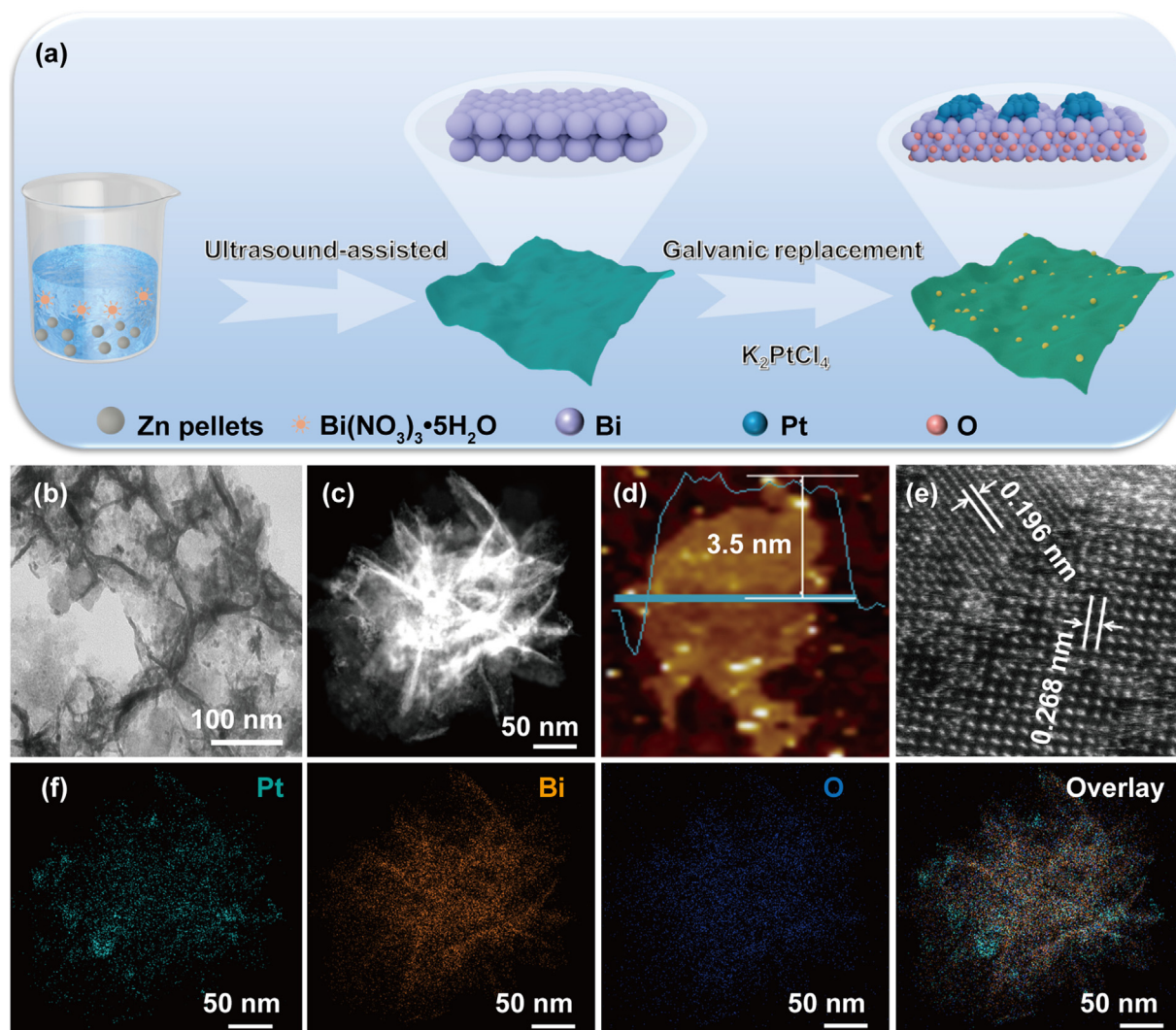*H.-Y. Yang et al.*　　　　　　　　　　　　　　　　　　　　　　　　　　　　　　　　

Fig. 1. Physical characterization of PtBi DONS. (a) Diagram of the preparation of PtBi DONS. (b) TEM image, (c) HAADF-STEM image, (d) AFM image, (e) HRTEM image, and (f) HAADF-STEM-EDX maps of Pt_1Bi_1 DONS.

result of Bi NS (Fig. S3 online) perfectly matches the standard JCPDS No. 44-1246 for pure Bi, proving that the Bi_2O_3 in Pt_1Bi_1 DONS is primarily produced through the galvanic replacement reaction. Such a structural arrangement suggests a decorated nanosheet morphology, where Pt NC are dispersed on the Bi_2O_3 NS surface, maintaining the integrity of the underlying oxide structure.

X-ray photoelectron spectroscopy (XPS) analysis was performed to investigate the chemical states and electronic structure of the constituent elements in Pt_1Bi_1 DONS (Fig. 2b). The deconvolution of the Pt 4f spectrum (Fig. 2c) reveals a characteristic doublet corresponding to the Pt $4f_{7/2}$ and Pt $4f_{5/2}$ core levels, with binding energies of 70.62 and 73.94 eV, respectively. These values represent a notable downward shift of 0.48 eV compared to that of bulk metallic Pt (typically 71.1 eV for Pt $4f_{7/2}$), which indicates the electron enrichment of Pt NC [34]. Furthermore, XPS analysis reveals that the majority of Pt exists in its metallic state (Pt^0), as evidenced by the relatively smaller peak areas corresponding to Pt^{2+} in comparison to those observed for cPt NC. The significant reduction in the Pt^{2+} peak area for Pt_1Bi_1 DONS catalysts highlights the role of the Bi_2O_3 support in stabilizing Pt and suppressing surface oxidation (Fig. S4 online). The Bi 4f spectrum (Fig. 2d) exhibits the peaks at binding energies of 158.73 eV (Bi $4f_{7/2}$) and 164.04 eV (Bi $4f_{5/2}$)

with a slight positive shift of 0.13 eV, further demonstrating the reduced electron density of Bi^{3+} in Bi_2O_3 [35]. The observed binding energy downshift in the Pt 4f spectrum, coupled with the positive shift of Bi 4f binding energies, indicates that the electron transfer between Pt and Bi_2O_3, where Pt acts as an electron acceptor from Bi_2O_3 NS. In addition, the lower oxygen vacancy:lattice oxygen ($O_V:O_L$) ratio in Pt_1Bi_1 DONS compared to Pt_1Bi_3 DONS demonstrates an optimized balance to effective stabilization of Bi in its oxidized state (Fig. S5 online).

The increased electron density around Pt atoms is also analyzed using extended X-ray absorption fine structure (EXAFS). The Pt L_3-edge X-ray absorption near-edge structure (XANES) spectra for Pt foil, Pt_1Bi_1 DONS, and PtO_2 (Fig. 2e) demonstrate that the absorption position of Pt_1Bi_1 DONS is close to that of the Pt foil [36,37]. The slightly higher white line intensity of the Pt_1Bi_1 DONS indicates the light oxidation state of Pt in Pt_1Bi_1 DONS, which aligns with the XPS results [38]. The R-space Fourier-transform extended X-ray absorption fine structure (FT-EXAFS, Fig. 2f) spectrum of Pt in Pt_1Bi_1 DONS provides further insights, showing a dominant peak at ~2.42 Å corresponding to the Pt–Pt bond, further demonstrating that Pt in Pt_1Bi_1 DONS is in the metallic Pt^0 form. The Pt–Pt bond strength in Pt_1Bi_1 DONS is significantly weakened compared to that in Pt foil, indicating that Pt atoms are highly dispersed on the Bi_2O_3
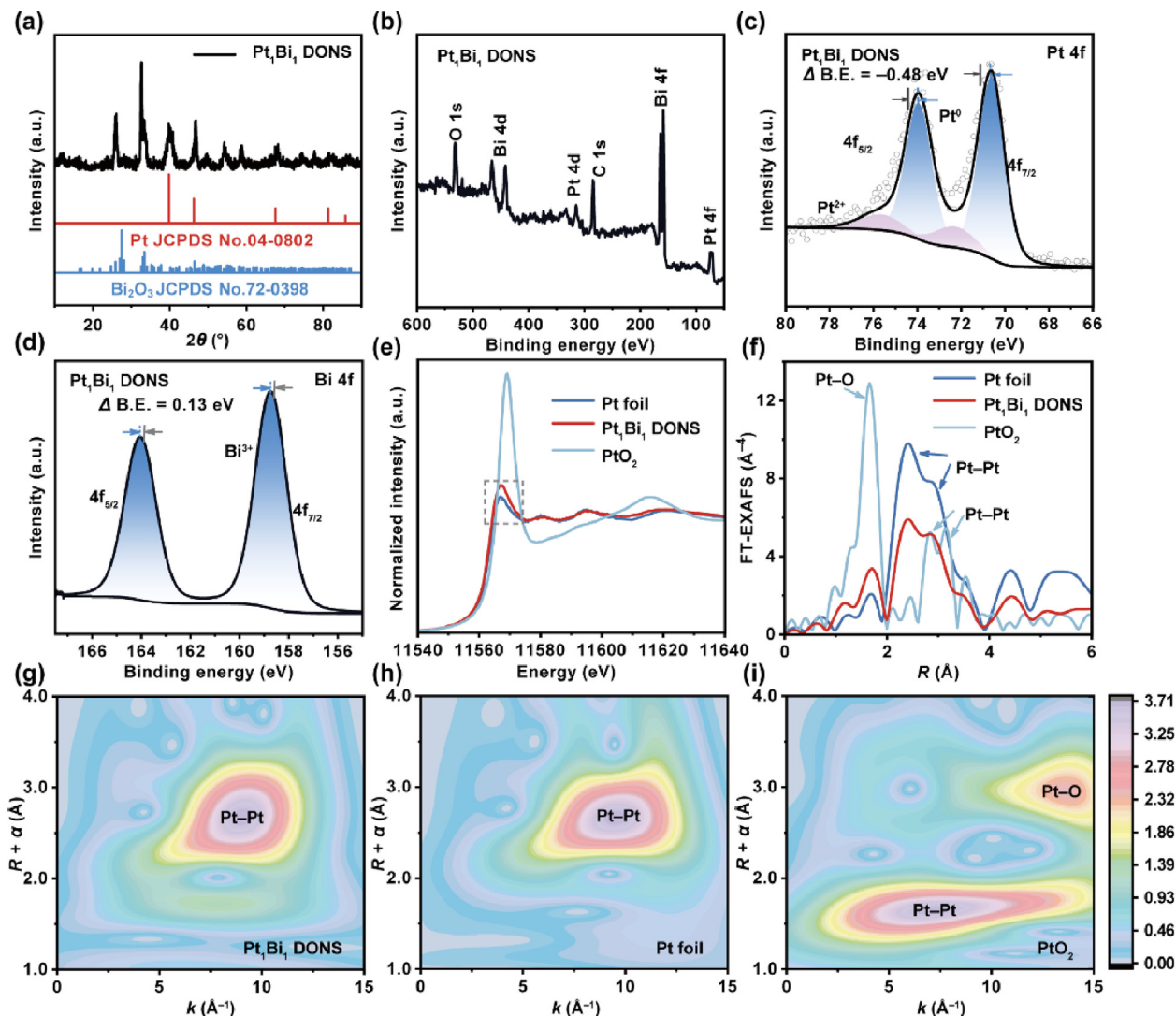
Fig. 2. XRD and chemical characterization of PtBi DONS. (a) XRD pattern of Pt_1Bi_1 DONS. (b) XPS survey spectrum. (c) Pt 4f XPS spectrum and (d) Bi 4f XPS spectrum of Pt_1Bi_1 DONS ($\Delta B.E.$: Binding energy offset). (e) Normalized Pt L_3-edge XANES for Pt foil, Pt_1Bi_1 DONS, and PtO_2. (f) FT-EXAFS spectra of Pt in Pt foil, Pt_1Bi_1 DONS, and PtO_2. (g–i) WT-EXAFS spectra of Pt in Pt_1Bi_1 DONS, Pt foil, and PtO_2.

nanosheets [16,39]. Unlike PtO_2, no notable Pt–O bond is observed in the Pt_1Bi_1 DONS. Furthermore, the wavelet transforms (WT-EXAFS, Figs. 2g–i) of Pt foils, Pt_1Bi_1 DONS, and PtO_2 elucidate the coordination environments of Pt in Pt_1Bi_1 DONS. WT-EXAFS spectra at the Pt L_3-edge for Pt_1Bi_1 DONS indicate a maximum intensity at ~2.67 Å, 9.05 Å^{-1}, attributed to the electron dispersion and enrichment [40,41], distinct from those of Pt foil (Pt–Pt: 2.65 Å, 9.5 Å^{-1}) and PtO_2 (Pt–O: 1.65 Å, 7.25 Å^{-1}). This further confirms the unique electronic structure of Pt within Pt_1Bi_1 DONS [42]. To further illustrate the electronic structure of Pt_1Bi_1 DONS, computational simulation of charge density differences (Fig. S6 online) confirms that the electrons are transferred from Bi_2O_3 to Pt.

3.2. Activity and selectivity of Pt_1Bi_1 DONS for GOR

The electrocatalytic activity of the Pt-doped Bi_2O_3 nanosheets for GOR was systematically evaluated under alkaline solution using a three-electrode system. A comprehensive investigation of the electrocatalytic performance was conducted by systematically varying the glycerol concentration from 50 mmol L^{-1} to 1.0 mol L^{-1} to understand its impact on the catalytic behavior. Linear sweep voltammetry (LSV) results (Fig. 3a) reveal a systematic negative

shift in the onset potential with increasing glycerol concentration. Notably, the relationship between glycerol concentration and current density followed a nonmonotonic trend. As the concentration increased from 50 mmol L^{-1} to 0.5 mol L^{-1}, a significant enhancement in current density is observed, and the onset potential negatively shifts from 0.46 to 0.35 V vs. RHE. However, a further increase to 1.0 mol L^{-1} results in a negligible increase in performance. Thus, the optimal current is achieved at 0.5 mol L^{-1} glycerol, suggesting a balance between reactant availability and mass transport efficiency. Consequently, 0.5 mol L^{-1} glycerol is selected for subsequent electrochemical characterizations. Notably, the control experiments are conducted in the absence of glycerol, where Pt_1Bi_1 DONS exhibit negligible current response, confirming the specificity of Pt_1Bi_1 DONS for catalyzing glycerol oxidation.

To determine the optimal Pt/Bi ratio, LSV curves (Fig. 3b) were obtained for Pt_1Bi_1 DONS, cPt NC, and Pt_1Bi_3 DONS (Figs. S7 and S8 online). The characterization results (Figs. S9–S11 online) of Pt_1Bi_3 DONS confirm that the morphology is similar to Pt_1Bi_1 DONS and the Pt/Bi ratio is ~1:3, respectively. When operating at a current of 200 mA mg$_{cat}^{-1}$, Pt_1Bi_1 DONS achieve a potential of 0.53 V vs. RHE, demonstrating superior electrocatalytic performance compared to both Pt_1Bi_3 DONS (0.59 V vs. RHE) and cPt NC (0.65 V
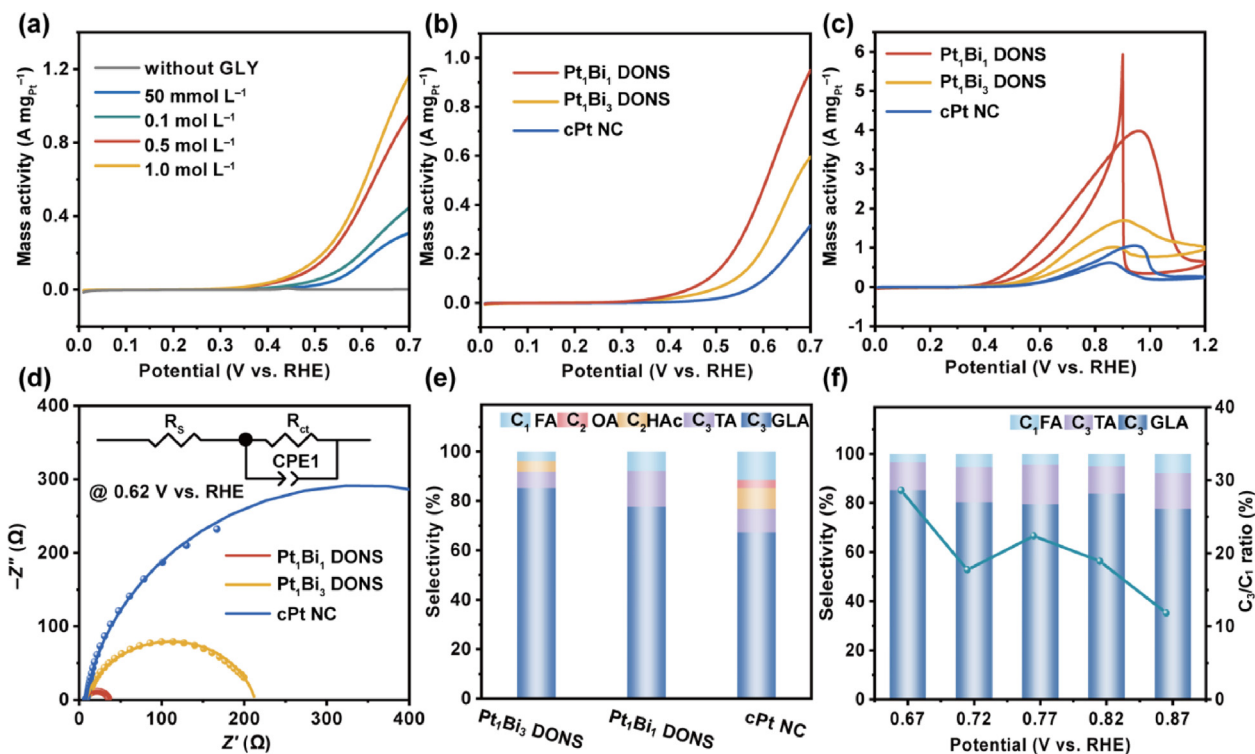
Fig. 3. GOR performances of Pt_1Bi_1 DONS, Pt_1Bi_3 DONS, and cPt NC in an alkaline electrolyte. (a) LSV curves of Pt_1Bi_1 DONS in N_2-purged 1 mol L^{-1} KOH without and with different concentrations of glycerol. (b) LSV curves of Pt_1Bi_1 DONS, Pt_1Bi_3 DONS, and cPt NC in N_2-purged 1 mol L^{-1} KOH + 0.5 mol L^{-1} glycerol. (c) CV curves of Pt_1Bi_1 DONS, Pt_1Bi_3 DONS, and cPt NC in N_2-purged 1 mol L^{-1} KOH with 0.5 mol L^{-1} glycerol addition. (d) Nyquist plots of Pt_1Bi_1 DONS, Pt_1Bi_3 DONS, and cPt NC. (e) C_3 product selectivity of Pt_1Bi_1 DONS, Pt_1Bi_3 DONS, and cPt NC. (f) C_3 product selectivity and C_3/C_1 ratio of Pt_1Bi_1 DONS at varied potentials.

vs. RHE). Cyclic voltammetry (CV) studies (Fig. 3c) corroborate the LSV findings. The GOR peak currents follow the order of Pt_1Bi_1 DONS > Pt_1Bi_3 DONS > cPt NC. Exhibiting a GOR mass activity of 3.98 A mg_{Pt}^{-1} at peak potential, Pt_1Bi_1 DONS surpasses cPt NC by 3.8-fold and Pt_1Bi_3 DONS by 2.4-fold, underscoring the optimal Pt:Bi ratio to be ~1:1 to maximize catalytic activity. In addition, the distinctively larger inverse peak observed for Pt_1Bi_1 DONS reflects the synergistic interactions between Pt and Bi_2O_3 that foster extensive oxide formation and reduction cycles, ultimately enhancing the regeneration of active sites and resulting in superior catalytic performance. To elucidate the kinetic aspects of the catalytic process, electrochemical impedance spectroscopy (EIS) tests were employed. Nyquist plots (Fig. 3d) reveal that Pt_1Bi_1 DONS exhibit the smallest charge transfer resistance among Pt_1Bi_3 DONS and cPt NC. The enhanced electron transfer kinetics at the electrode-electrolyte interface correlate well with the enhanced catalytic activity observed in LSV and CV measurements.

The oxidation products were characterized both qualitatively and quantitatively using the complementary analytic techniques ^1H NMR spectra (Fig. S12 online) and HPLC (Figs. S13–S16 and Table S1 online) across different electrocatalysts. Pt_1Bi_1 DONS demonstrates superior selectivity of 92.2% for the C_3 products at a potential of 0.87 V vs. RHE, suggesting that the optimal Pt:Bi ratio in Pt_1Bi_1 DONS promotes the preservation of the carbon skeleton during GOR (Fig. 3e). By contrast, Pt_1Bi_3 DONS and cPt NC exhibit significantly lower selectivities of 91.8% and 76.8% for the C_3 products, respectively, yielding a more diverse array of oxidation products, such as the C_1 product (FA) and C_2 products (OA and HAc). The enhanced C_3 selectivity is attributed to the optimal electronic structure resulting from the interaction between Pt and Bi_2O_3 in Pt_1Bi_1 DONS. Given the notable influence of applied potential on GOR, we conducted characterization of the oxidation products generated by Pt_1Bi_1 DONS at varied potentials (Fig. 3f). At lower poten-

tials, the C_3 products predominate, indicating preferential oxidation of primary alcohol groups without C–C bond cleavage [43]. As the potential increases, the selectivity for C_3 products gradually decreases from 96.6% to 92.2%, indicating the onset of C–C bond cleavage. The observed decline in C_3 selectivity with increasing potential can be explained by the enhanced C–C bond scission, which occurs as the electrocatalyst surface adopts a higher oxidation state [44]. The timed current test (amperometry i-t curves, AC) (Fig. S17 online) indicates that the Pt_1Bi_1 DONS exhibit good stability, which is better than cPt NC. The postreaction characterization data of SEM (Fig. S18 online), TEM (Fig. S19 online), and XPS (Fig. S20 online) confirm that the Pt_1Bi_1 DONS retain their original morphological features and chemical states, demonstrating excellent structural and chemical stability under electrochemical conditions during the GOR.

3.3. The role of Bi_2O_3 in Pt_1Bi_1 DONS of GOR

To elucidate the role of Bi_2O_3 in Pt_1Bi_1 DONS, we compared the activity and selectivity of Pt_1Bi_1 DONS, PtBi nanosheets (PtBi NS), Bi_2O_3 nanosheets (Bi_2O_3 NS) (Figs. S21 and S22 online), and Bi nanosheets (Bi NS) during GOR. The characterization data of PtBi NS (Figs. S23–S25 online) confirms the formation of hexagonal nanosheet structures with a Pt:Bi atomic ratio of ~1:1, as corroborated by EDS analysis and XRD patterns matching the PtBi intermetallic nanosheets (JCPDS No. 97-061-6981). The CV result (Fig. 4a) shows the significantly higher peak mass activity of Pt_1Bi_1 DONS (3.98 A mg_{Pt}^{-1}) than PtBi NS (1.93 A mg_{Pt}^{-1}), with an earlier onset potential indicative of superior efficiency in initiating the GOR. From the LSV curves (Fig. 4b), Pt_1Bi_1 DONS distinctly outperform all other catalysts, underscoring the synergistic effect between Pt and Bi_2O_3, which is absent in both PtBi NS and Bi_2O_3 NS. Furthermore, Pt_1Bi_1 DONS exhibit a lower resistance during
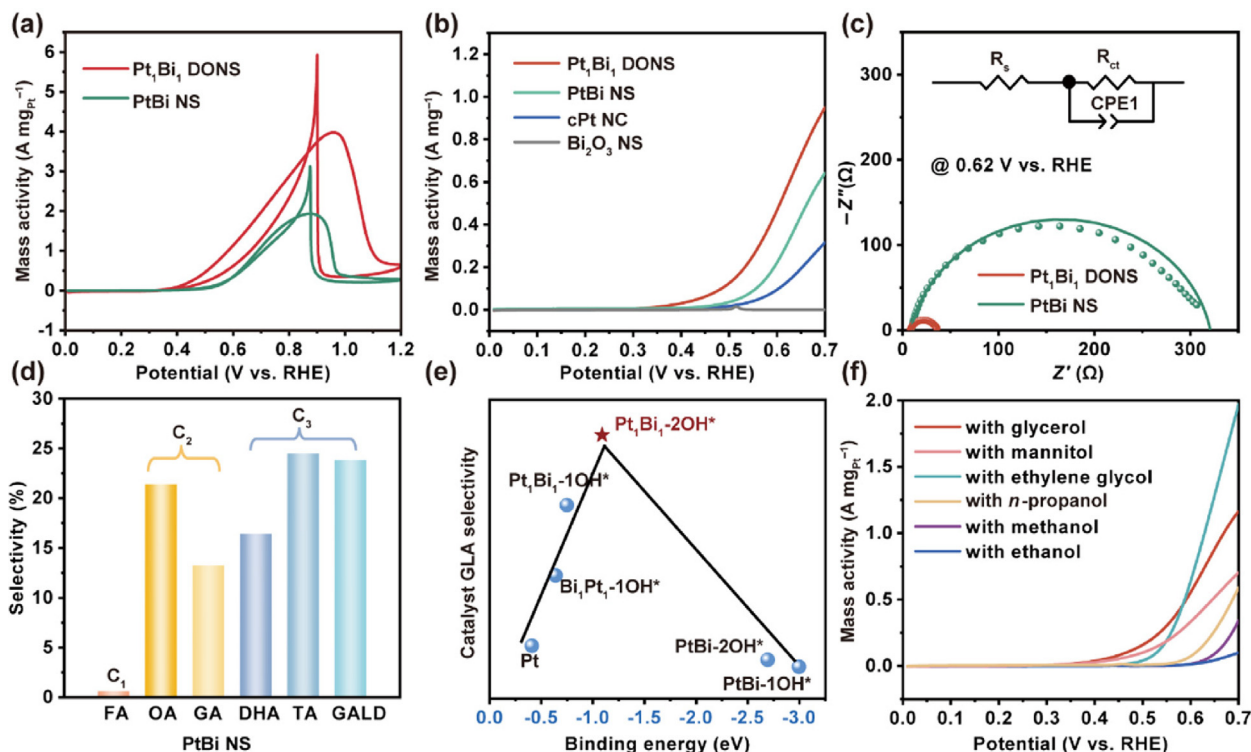
Fig. 4. GOR performances of Pt₁Bi₁ DONS, PtBi NS, and Bi₂O₃ NS in an alkaline electrolyte, DFT results of different adsorption configurations, and Pt₁Bi₁ DONS performance of catalytic polyols. (a) CV curves of Pt₁Bi₁ DONS and PtBi NS in N_2-purged 1 mol L^{-1} KOH + 0.5 mol L^{-1} glycerol. (b) LSV curves of Pt₁Bi₁ DONS, PtBi NS, cPt NC, and Bi₂O₃ NS in N_2-purged 1 mol L^{-1} KOH + 0.5 mol L^{-1} glycerol. (c) Nyquist plots of Pt₁Bi₁ DONS and PtBi NS. (d) C₃ product selectivity of PtBi NS at 0.87 V vs. RHE. (e) Binding energy of glycerol (OH species) and the GLA production rates for Pt₁Bi₁ DONS, PtBi NS, and cPt NC. (f) LSV curves of Pt₁Bi₁ DONS in N_2-purged 1 mol L^{-1} KOH with glycerol, mannitol, ethylene glycol, *n*-propanol, methanol, and ethanol.

GOR than PtBi NS (Fig. 4c), reflecting enhanced charge transfer kinetics facilitated by the unique Pt-Bi₂O₃ interface. The product distribution from GOR catalyzed by PtBi NS (Fig. 4d) was also determined using HPLC (Figs. S26 and S27 and Table S2 online), revealing distinct differences in selectivity. For Pt₁Bi₁ DONS, GLA was the predominant product. By contrast, PtBi NS generated a broader range of products, including C₁ to C₃, with a considerable contribution of DHA, a C₃ product notably absent in Pt₁Bi₁ DONS catalytic reaction. These comparisons highlight the critical role of the Bi₂O₃ in Pt₁Bi₁ DONS, which not only fine-tunes the electronic structure of Pt to facilitate C₃-selective production but also enhances the specified production of GLA.

To further verify the function of Bi₂O₃, the CV measurement was conducted on Bi₂O₃ NS (Fig. S28 online). The results exhibit a characteristic oxidation peak at 0.56 V vs. RHE in N_2-saturated 1 mol L^{-1} KOH solution during the CV scan (blue curve). However, on introducing 0.5 mol L^{-1} glycerol, both the oxidation peak and reduction peaks were completely suppressed (green curve), indicating that the OH$_{ads}$ species from glycerol preferentially adsorb on the Bi₂O₃ surface, subsequently blocking the Bi₂O₃ adsorption sites. Supported by the LSV data (Fig. 4b) showing negligible current for Bi₂O₃ NS in the presence of glycerol, it is evident that Bi₂O₃ NS lack intrinsic GOR capability. Thus, the primary role of Bi₂O₃ NS is to provide adsorption sites for glycerol, thereby enhancing oxidation through synergistic interactions with Pt. The volcano plot (Fig. 4e) derived from density functional theory (DFT) calculations (Fig. S29 online) illustrates the correlation between the binding energy of glycerol (OH species) and the GLA production rate for various catalytic surfaces, including Pt₁Bi₁ DONS, PtBi NS, and Pt. Two distinct adsorption configurations are considered namely the lying-down configuration (2OH*) and the standing configuration (1OH*). Pt₁Bi₁ DONS with the lying configuration (Pt₁Bi₁-

2OH*) reside at the volcano's peak, signifying the highest catalytic activity and optimal binding energy. This configuration facilitates the formation of GLA due to the simultaneous interaction of two hydroxyl groups with the catalyst surface. Conversely, the standing configuration calculated for Pt₁Bi₁ DONS and PtBi NS displays a lower activity as it binds too weakly or too strongly. Interestingly, glycerol demonstrates a strong preference for the lying configuration on Pt₁Bi₁ DONS, whereas the standing configuration is favored on PtBi NS. The preferential adsorption configuration on Pt₁Bi₁ DONS enhances the selective production of GLA, emphasizing the critical role of Bi₂O₃ in modulating the Pt binding environment and steering glycerol oxidation toward GLA rather than DHA.

Considering the function of Bi₂O₃ for tuning the adsorption of OH$_{ads}$, we extend the testing of Pt₁Bi₁ DONS against other multicarbon alcohols, namely ethylene glycol (EG), mannitol, *n*-propanol, methanol, and ethanol. LSV curves (Fig. 4f) compare the performances of Pt₁Bi₁ DONS in the oxidation of polyols and monoalcohols. Notably, Pt₁Bi₁ DONS exhibit considerably higher currents and more negative onset potentials for polyols (EG and mannitol) than monoalcohols (*n*-propanol, methanol, and ethanol). The CV tests (Fig. S30 online) further demonstrate the consistent role of Bi₂O₃ NS across all tested polyols, with oxidation and reduction peaks completely suppressed due to the strong adsorption of polyols on Bi₂O₃ NS, whereas these peaks remain observable with monoalcohols. This adsorption behavior of the Bi₂O₃ NS confers versatility upon the Pt₁Bi₁ DONS by providing effective sites for diverse polyols, which stabilize reaction intermediates and enhance catalytic activity. Such adaptability underscores the crucial Pt and Bi₂O₃ synergy, extending the notable electrocatalytic performance of the catalyst from glycerol oxidation to a wider spectrum of polyols.

3.4. The reaction mechanism of GOR

To further elucidate the enhanced catalytic activity over Pt_1Bi_1 DONS, *operando* EIS was employed to study the GOR process, providing insights into the electrode and electrolyte interface properties. The Bode plots for Pt_1Bi_1 DONS (Fig. 5a) reveal a narrow single peak across the frequency spectrum, indicative of a more uniform and accelerated charge transfer process, which suggests enhanced kinetics for surface OH_{ads} adsorption and subsequent interaction with glycerol molecules [45]. Compared to Pt_1Bi_3 DONS and cPt NC, Pt_1Bi_1 DONS exhibit lower phase angles, which in EIS typically denotes less resistive behavior [22]. In this context, it implies faster reaction kinetics and facilitated charge transfer, corroborating the earlier EIS observations (Fig. 3d). By contrast, cPt NC (Fig. 5b) display a bimodal response with distinct low and high-frequency peaks, while Pt_1Bi_1 DONS demonstrate a simplified impedance profile [46]. The 1:1 ratio of Pt:Bi optimizes the surface for OH_{ads} adsorption and its reaction with glycerol, potentially streamlining the reaction mechanism.

While Pt_1Bi_3 DONS (Fig. S31 online) also show enhancements compared to cPt NC, the comparatively lower phase angles and the broader peak of Pt_1Bi_1 DONS indicate that the 1:1 ratio achieves an optimal balance for OH_{ads} adsorption and utilization in the GOR. Moreover, Pt_1Bi_3 DONS exhibit a more pronounced peak in the midfrequency range, suggesting increased capacitive

behavior [47]. The pronounced peak can be attributed to higher Bi content, leading to stronger adsorption of reaction intermediates or a more developed electrical double layer. However, the higher phase angles observed in Pt_1Bi_3 DONS relative to Pt_1Bi_1 DONS imply slower charge transfer kinetics, indicating that while increasing Bi content enhances OH_{ads} adsorption, it may simultaneously inhibit the subsequent reaction steps through stronger intermediate binding. By contrast, the Bode plots of PtBi NS (Fig. S32 online) display an even broader peak than that of Pt_1Bi_1 DONS, suggesting multiple overlapping kinetic processes. The broader peak indicates less efficient charge transfer dynamics and increased intermediate accumulation on the catalyst surface, likely arising from the PtBi NS lack of Bi_2O_3, which is optimized for efficient OH_{ads} modulation in Pt_1Bi_1 DONS.

The arrangement of functional groups within small organic molecules markedly influences their reaction mechanisms. In the context of alkaline GOR, where coadsorption of hydroxide ions and glycerol occurs, the behavior of *n*-propanol, which maintains the same concentration of hydroxyl groups, was also studied on Pt_1Bi_1 DONS (Fig. 5c). During GOR, the response of Pt_1Bi_1 DONS exhibits narrower peaks that shifted toward higher frequencies, indicating a relatively uniform process with a fast charge transfer rate. By contrast, the oxidation of *n*-propanol results in broader peaks, more prominently centered around lower frequencies, suggesting a more complex process with significant resistance at the
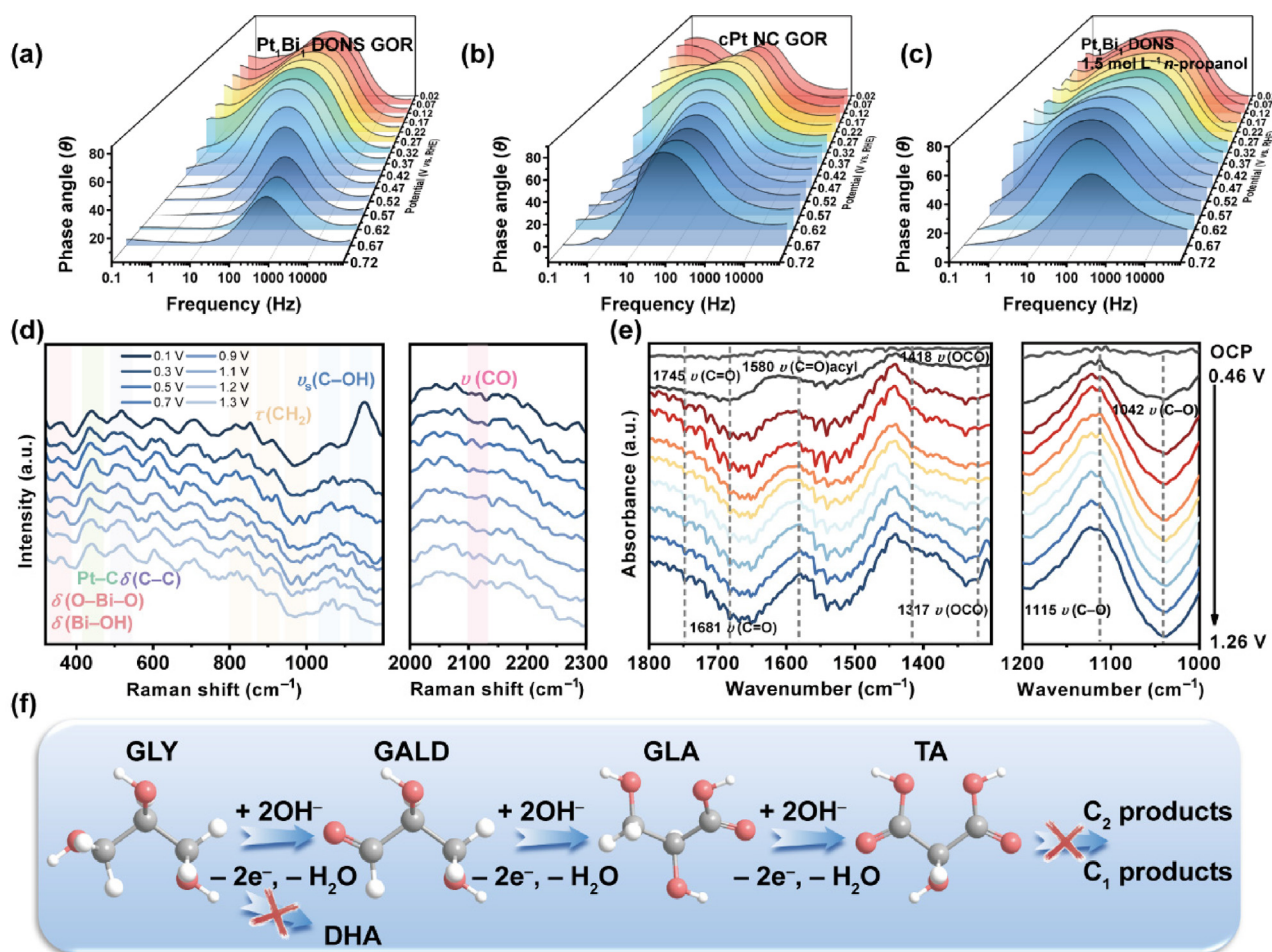

Fig. 5. *In situ* characterizations and illustration of the mechanism and reaction process. Bode plots of (a) Pt_1Bi_1 DONS and (b) cPt NC in 1 mol L^{-1} KOH + 0.5 mol L^{-1} glycerol. (c) Bode plots of Pt_1Bi_1 DONS in 1 mol L^{-1} KOH + 1.5 mol L^{-1} *n*–propanol. (d) Electrochemical *in situ* Raman spectral evolution of Pt_1Bi_1 DONS at different potentials in 1 mol L^{-1} KOH + 0.5 mol L^{-1} glycerol. (e) Electrochemical *in situ* FTIR spectra of Pt_1Bi_1 DONS at different potentials in 1 mol L^{-1} KOH + 0.1 mol L^{-1} glycerol. (f) Scheme of the GOR reaction pathway.

molecular adsorption site. Glycerol, with three hydroxyl groups, contains multiple adsorption sites, leading to a stable adsorption configuration. Conversely, *n*-propanol displays varied adsorption configurations, resulting in the formation of adsorbed reactants and intermediates with diverse binding strengths. The presence of Bi_2O_3 facilitates a stable conformation for polyols such as glycerol, wherein multiple hydroxyl groups are adsorbed on Pt_1Bi_1 DONS. This not only simplifies the reaction pathway but also enhances hydroxyl activation of the polyols, reducing reliance on hydroxyl ions in solution, which elucidates why polyols generally outperform monoalcohols in the LSV curves (Fig. 4f).

To investigate the GOR kinetics at Pt_1Bi_1 DONS, electrochemical *in situ* Raman spectroscopy was applied (Fig. 5d), revealing the characteristic vibrational modes of glycerol and its oxidation intermediates. The spectral analysis shows intensive peaks in the 800–1000 cm^{-1} region, which are attributed to the $\tau(CH_2)$ vibrations of the glycerol [48]. The distinct bands around 1050 and 1109 cm^{-1} are assigned to the $v_s(C–OH)$ modes associated with the terminal and intermediate carbon atoms of glycerol, respectively [49]. Notably, the vibrational peaks at 1088–1130 cm^{-1} diminish with increasing potential, indicating the consumption of the –OH groups on intermediate carbon atoms. By contrast, the intensity of the peaks at 1020–1080 cm^{-1} remains relatively constant, suggesting that the –OH groups on the terminal carbon atoms are not significantly consumed. The peaks below 400 cm^{-1}, attributed to OH_{ads} adsorbed on Bi, suggest a favorable environment for OH_{ads} adsorption, with their intensities slightly decreasing as the potential increases. This behavior implies that the –OH groups adsorbed during polyol oxidation likely originate from the structure of glycerol rather than external sources. In addition, the C–C vibrational mode at 518 cm^{-1} exhibits minor changes, indicating variations in the adsorption geometries of glycerol and its intermediates. Notably, the Pt–C stretching peak at 438 cm^{-1} remains relatively constant across the potential range, indicating the preservation of C–C bonds [50]. The stability is likely due to the electron-rich Pt environment enhanced by Bi_2O_3, which effectively reduces C–C bond cleavage and thus improves the C_3 selectivity of Pt_1Bi_1 DONS. A slight increase in the CO peak intensity (~2110 cm^{-1}) is observed at higher potentials [51], consistent with the minor decrease in C_3 product selectivity at elevated potentials (Fig. 3f).

The reaction intermediates were monitored using *in situ* Fourier-transform infrared (*in-situ* FTIR) spectroscopy (Fig. 5e). The spectral analysis reveals characteristic peaks at 1317 and 1400 cm^{-1}, attributed to the symmetric carboxylate group stretching modes, alongside a peak at 1580 cm^{-1}, which is assigned to the asymmetric carboxylate stretching [52]. Additionally, a distinct vibrational feature at 1745 cm^{-1} is attributed to the C=O stretching of carboxylic acids or aldehydes [53–55]. As the applied potential increases, the intensities of these peaks increase, signifying the formation of GLA as the predominant product over the tested potential range. By contrast, the peaks at 1032 and 1145 cm^{-1} are associated with the C–O stretching vibrations [25]. Notably, the persistence of C–O peaks at elevated potential indicates partial oxidation of glycerol [56], suggesting a high likelihood of preserving the C_3 structure. The electron-rich nature of Pt in Pt_1Bi_1 facilitates controlled partial oxidation, preventing extensive C–C bond cleavage and promoting selective production.

Therefore, the reaction pathway for glycerol oxidation on Pt_1Bi_1 DONS, as shown in Fig. 5f, is a stepwise oxidation process culminating in the formation of tartronic acid. First, glycerol undergoes successive oxidation steps, each involving the loss of two electrons and protons coupled with the addition of hydroxyl ions. This progression leads to the formation of glyceraldehyde, which subsequently oxidizes to GLA, thereby maintaining the original C_3 carbon skeleton. It is noteworthy that the selectivity for C_3 products can be attributed to the unique electronic properties of Pt_1Bi_1

DONS, where the electron-rich Pt facilitates controlled oxidation. Meanwhile, the presence of Bi_2O_3 for the adsorption of the –OH groups in polyols, which changes the adsorption configuration, results in the selective production of GLA.

4. Conclusion

Herein, Pt_1Bi_1 DONS were developed to achieve a highly selective yield of C_3 value-added products during GOR. Pt_1Bi_1 DONS demonstrate notable performance, delivering a current of 0.82 A mg^{-1} at 0.67 V vs. RHE and achieving an impressive GLA selectivity of 88.3% and an overall C_3 selectivity of 96.6% across a broad potential range. Uniquely, Pt_1Bi_1 DONS facilitate a pathway exclusively converting glycerol to GLA, as opposed to Pt_1Bi_3 DONS and cPt NC, where additional pathways are active. Both experimental and theoretical analyses reveal that the electron-rich nature of Pt diminishes its propensity to cleave C–C bonds, thus curtailing the formation of C_2/C_1 products. In addition, the adsorption configuration of glycerol is critical in determining the product profile, suggesting that the adsorption configuration optimized by Bi_2O_3 NS can further modulate reaction pathways and thus favor GLA production. This study introduces high-performance Pt_1Bi_1 DONS for converting glycerol into C_3 products and elucidates the mechanisms behind their enhanced activity, proposing that the influence of Bi_2O_3 on the polyol adsorption configuration can be pivotal in directing reaction pathways.

Conflict of interest

The authors declare that they have no conflict of interest.

Author contributions

Han-Yue Yang contributed to the conceptualization, data curation, formal analysis, methodology, and writing of the original draft. Bin Sun performed the formal analysis. Xue Xiao participated in the conceptualization, formal analysis, original draft writing, and manuscript review and editing. Xuan Ai, Rui-Bin Jiang, and Pei Chen provided supervision and contributed to manuscript review and editing. Yu Chen contributed to the validation, supervision, funding acquisition, and manuscript review and editing.

Appendix A. Supplementary material

Supplementary data to this article can be found online at https://doi.org/10.1016/j.scib.2025.05.032.

References

[1] Pagliaro M, Ciriminna R, Kimura H, et al. From glycerol to value-added products. Angew Chem Int Edit 2007;46:4434–40.

[2] Sharninghausen LS, Campos J, Manas MG, et al. Efficient selective and atom economic catalytic conversion of glycerol to lactic acid. Nat Commun 2014;5:5084.

[3] Gallezot P. Conversion of biomass to selected chemical products. Chem Soc Rev 2012;41:1538–58.

[4] Wu LY, Wu QL, Han Y, et al. Strengthening the synergy between oxygen vacancies in electrocatalysts for efficient glycerol electrooxidation. Adv Mater 2024;36:e2401857.

[5] Chu S, Majumdar A. Opportunities and challenges for a sustainable energy future. Nature 2012;488:294–303.

[6] Lin C, Lu Y, Miao JM, et al. Quasi-homogeneous photoelectrochemical organic transformations for tunable products and 100% conversion ratio. Sci Bull 2024;69:3395–403.

[7] Liao YH, Koelewijn SF, Bossche GV, et al. A sustainable wood biorefinery for low-carbon footprint chemicals production. Science 2020;367:1385–90.

[8] Fan RY, Zhai XJ, Qiao WZ, et al. Optimized electronic modification of s-doped CuO induced by oxidative reconstruction for coupling glycerol electrooxidation with hydrogen evolution. Nano-Micro Lett 2023;15:190.

[9] Lyu NX, Chen YS, Guan AX, et al. Electrocatalytic glycerol upgrading into glyceric acid on Ni3Sn intermetallic compound. Small 2024;20:e2401872.

[10] Sheng HY, Janes AN, Ross RD, et al. Linear paired electrochemical valorization of glycerol enabled by the electro-Fenton process using a stable NiSe2 cathode. Nat Catal 2022;5:716–25.

[11] Dodekatos G, Schünemann S, Tüysüz H. Recent advances in thermo-, photo-, and electrocatalytic glycerol oxidation. ACS Catal 2018;8:6301–33.

[12] Goetz MK, Usman E, Choi KS. Understanding and suppressing C–C cleavage during glycerol oxidation for C3 chemical production. ACS Catal 2023;13:15758–69.

[13] Corma A, Iborra S, Velty A. Chemical routes for the transformation of biomass into chemicals. Chem Rev 2007;107:2411–502.

[14] Li SL, Liu DM, Wang GW, et al. Vertical 3D nanostructures boost efficient hydrogen production coupled with glycerol oxidation under alkaline conditions. Nano-Micro Lett 2023;15:189.

[15] Zhou YF, Shen Y, Xi JY. Seed-mediated synthesis of Pt$_x$Au$_y$@Ag electrocatalysts for the selective oxidation of glycerol. Appl Catal B 2019;245:604–12.

[16] Li Y, Wei XF, Pan R, et al. PtAu alloying-modulated hydroxyl and substrate adsorption for glycerol electrooxidation to C3 products. Energy Environ Sci 2024;17:4205–15.

[17] Zhang JB, Li XL, Xu M, et al. Glycerol aerobic oxidation to glyceric acid over Pt/hydrotalcite catalysts at room temperature. Sci Bull 2019;64:1764–72.

[18] Kwon Y, Schouten KJP, Koper MTM. Mechanism of the catalytic oxidation of glycerol on polycrystalline gold and platinum electrodes. ChemCatChem 2011;3:1176–85.

[19] Garcia AC, Kolb MJ, CvNY S, et al. Strong impact of platinum surface structure on primary and secondary alcohol oxidation during electro-oxidation of glycerol. ACS Catal 2016;6:4491–500.

[20] Yu XW, Santos EC, White J, et al. Electrocatalytic glycerol oxidation with concurrent hydrogen evolution utilizing an efficient MoO$_x$/Pt catalyst. Small 2021;17:e2104288.

[21] Akbar MS, Whittaker TN, Yun TY, et al. The role of surface hydroxyls in the entropy-driven adsorption and spillover of H2 on Au/TiO2 catalysts. Nat Catal 2023;6:710–9.

[22] Zhou P, Lv XS, Tao SS, et al. Heterogeneous-interface-enhanced adsorption of organic and hydroxyl for biomass electrooxidation. Adv Mater 2022;34:e2204089.

[23] Ham MPJMvd, Creus J, Bitter JH, et al. Electrochemical and non-electrochemical pathways in the electrocatalytic oxidation of monosaccharides and related sugar alcohols into valuable products. Chem Rev 2024;124:11915–61.

[24] Kim D, Lim WG, Kim Y, et al. Amorphous antimony oxide as reaction pathway modulator toward electrocatalytic glycerol oxidation for selective dihydroxyacetone production. Appl Catal B 2023;339:123104.

[25] Luo L, Chen WS, Xu SM, et al. Selective photoelectrocatalytic glycerol oxidation to dihydroxyacetone via enhanced middle hydroxyl adsorption over a Bi2O3–incorporated catalyst. J Am Chem Soc 2022;144:7720–30.

[26] Xia ZC, Ma CY, Fan Y, et al. Vacancy optimized coordination on nickel oxide for selective electrocatalytic oxidation of glycerol. ACS Catal 2024;14:1930–8.

[27] Lan B, Wang QL, Ma ZX, et al. Efficient electrochemical ethanol-to-CO2 conversion at rhodium and bismuth hydroxide interfaces. Appl Catal B 2022;300:120728.

[28] Huang YY, Cai JD, Guo YL. A high-efficiency microwave approach to synthesis of Bi-modified Pt nanoparticle catalysts for ethanol electro-oxidation in alkaline medium. Appl Catal B 2013;129:549–55.

[29] Feng SX, Yi J, Miura H, et al. Experimental and theoretical investigation of the role of bismuth in promoting the selective oxidation of glycerol over supported Pt–Bi catalyst under mild conditions. ACS Catal 2020;10:6071–83.

[30] de Souza MBC, Vicente RA, Yukuhiro VY, et al. Bi-modified Pt electrodes toward glycerol electrooxidation in alkaline solution: effects on activity and selectivity. ACS Catal 2019;9:5104–10.

[31] Deng BL, Shen J, Lu JX, et al. Ru doping triggering reconstruction of cobalt phosphide for coupling glycerol electrooxidation with seawater electrolysis. J Energy Chem 2024;100:317–26.

[32] Ren FF, Pan HJ, Wang C, et al. Combining bismuth telluride and palladium for high efficiency glycerol electrooxidation. ChemSusChem 2024;1:e202401682.

[33] Miao BQ, Fang WS, Sun B, et al. Defect-rich bismuth metallene for efficient CO2 electroconversion. Chin J Struct Chem 2023;42:100095.

[34] Yang LT, Hou S, Zhu SY. Stabilizing Pt electrocatalysts via introducing reducible oxide support as reservoir of electrons and oxygen species. ACS Catal 2022;12:13523–32.

[35] Wan YC, Zhou HJ, Zheng MY, et al. Oxidation state modulation of bismuth for efficient electrocatalytic nitrogen reduction to ammonia. Adv Funct Mater 2021;31:2100300.

[36] Huang ZL, Hu SN, Sun MZ, et al. Implanting oxophilic metal in PtRu nanowires for hydrogen oxidation catalysis. Nat Commun 2024;15:1097.

[37] Liu Y, Liu G, Chen XY, et al. Achieving negatively charged Pt single atoms on amorphous Ni(OH)2 nanosheets with promoted hydrogen absorption in hydrogen evolution. Nano-Micro Lett 2024;16:202.

[38] Rao P, Luo JM, Li J, et al. One-dimensional PtFe hollow nanochains for the efficient oxygen reduction reaction. Carbon Energy 2022;4:1003–10.

[39] Zhang MT, Li H, Chen JX, et al. Transition metal (Co, Ni, Fe, Cu) single-atom catalysts anchored on 3D nitrogen-doped porous carbon nanosheets as efficient oxygen reduction electrocatalysts for Zn-air battery. Small 2022;18:2202476.

[40] Wang Y, Wang MR, Mou XL, et al. Host-induced alteration of the neighbors of single platinum atoms enables selective and stable hydrogenation of butadiene. Nanoscale 2022;14:10506–13.

[41] Shi XJ, Huang Y, Bo YA, et al. Highly selective photocatalytic CO2 methanation with water vapor on single-atom platinum-decorated defective carbon nitride. Angew Chem Int Edit 2022;61:e202203063.

[42] Cai XL, Liu CH, Liu J, et al. Synergistic effects in cNTs-PdAu/Pt trimetallic nanoparticles with high electrocatalytic activity and stability. Nano-Micro Lett 2017;9:48.

[43] González-Cobos J, Baranton S, Coutanceau C. A systematic in situ infrared study of the electrooxidation of C3 alcohols on carbon-supported Pt and Pt–Bi catalysts. J Phys Chem C 2016;120:7155–64.

[44] Lee SO, Park M, Park YS, et al. How to change the reaction chemistry on nonprecious metal oxide nanostructure materials for electrocatalytic oxidation of biomass-derived glycerol to renewable chemicals. Adv Mater 2023;35:e2203285.

[45] Wang Y, Zhu YQ, Xie ZH, et al. Efficient electrocatalytic oxidation of glycerol via promoted OH* generation over single-atom-bismuth-doped spinel Co3O4. ACS Catal 2022;12:12432–43.

[46] Lu YX, Dong CL, Huang YC, et al. Identifying the geometric site dependence of spinel oxides for the electrooxidation of 5-hydroxymethylfurfural. Angew Chem Int Edit 2020;59:19215–21.

[47] Chen W, Xu LT, Zhu XR, et al. Unveiling the electrooxidation of urea: intramolecular coupling of the N–N bond. Angew Chem Int Edit 2021;60:7297–307.

[48] Liu C, Hirohara M, Maekawa T, et al. Selective electro-oxidation of glycerol to dihydroxyacetone by a non-precious electrocatalyst—CuO. Appl Catal B 2020;265:118543.

[49] Zalineeva A, Serov A, Padilla M, et al. Self-supported Pd$_x$Bi catalysts for the electrooxidation of glycerol in alkaline media. J Am Chem Soc 2014;136:3937–45.

[50] Nakamoto K. Infrared and raman spectra of inorganic and coordination compounds. Part A: theory and applications in inorganic chemistry. J Chem Educ 2000;77:149–354.

[51] An HY, de Ruiter J, Wu LF, et al. Spatiotemporal mapping of local heterogeneities during electrochemical carbon dioxide reduction. JACS Au 2023;3:1890–901.

[52] Zhang HN, Zhou P, Ji HW, et al. Enhancement of photocatalytic decarboxylation on TiO2 by water-induced change in adsorption-mode. Appl Catal B 2018;224:376–82.

[53] Zhang YN, Zhang XY, Yang PF, et al. In situ topologically induced PtZn alloy @ZnTiOx and the synergistic effect on glycerol oxidation. Appl Catal B 2021;298:120634.

[54] Chen W, Zhang L, Xu LT, et al. Pulse potential mediated selectivity for the electrocatalytic oxidation of glycerol to glyceric acid. Nat Commun 2024;15:2420.

[55] Huang L, Sun JY, Cao SH, et al. Combined EC-NMR and in situ FTIR spectroscopic studies of glycerol electrooxidation on Pt/C, PtRu/C, and PtRh/C. ACS Catal 2016;6:7686–95.

[56] Qi C, Bi YF, Wang YL, et al. Unveiling the mechanism of plasma-catalyzed oxidation of methane to C$_{2+}$ oxygenates over Cu/UiO-66-NH2. ACS Catal 2024;14:7707–16.